

# Beyond Scalars: Concept-Based Alignment Analysis in Vision Transformers

Johanna Vielhaben<sup>1</sup>

Dilyara Bareeva<sup>1</sup>

Jim Berend<sup>1</sup>

Wojciech Samek<sup>1,2,3,†</sup>

Nils Strothoff<sup>4,†</sup>

<sup>1</sup> Fraunhofer Heinrich-Hertz-Institute Berlin <sup>2</sup> Technische Universität Berlin <sup>3</sup> BIFOLD – Berlin Institute for the Foundations of Learning and Data

<sup>4</sup> Carl von Ossietzky Universität Oldenburg <sup>†</sup> corresponding authors: wojciech.samek@hhi.fraunhofer.de, nils.strothoff@uol.de

## Abstract

Vision transformers (ViTs) [10] can be trained using various learning paradigms, from fully supervised to self-supervised. Diverse training protocols often result in significantly different feature spaces, which are usually compared through alignment analysis. However, current alignment measures quantify this relationship in terms of a single scalar value, obscuring the distinctions between common and unique features in pairs of representations that share the same scalar alignment. We address this limitation by combining alignment analysis with concept discovery, which enables a breakdown of alignment into single concepts encoded in feature space. This fine-grained comparison reveals both universal and unique concepts across different representations, as well as the internal structure of concepts within each of them. Our methodological contributions address two key prerequisites for concept-based alignment: 1) For a description of the representation in terms of concepts that faithfully capture the geometry of the feature space, we define concepts as the most general structure they can possibly form - arbitrary manifolds, allowing hidden features to be described by their proximity to these manifolds. 2) To measure distances between concept proximity scores of two representations, we use a generalized Rand index and partition it for alignment between pairs of concepts. We confirm the superiority of our novel concept definition for alignment analysis over existing linear baselines in a sanity check. The concept-based alignment analysis of representations from four different ViTs reveals that increased supervision correlates with a reduction in the semantic structure of learned representations.

## 1. Introduction

Vision Transformers are gaining increased popularity as backbones for various computer vision tasks. There is a large zoo of pre-trained models trained with various learning paradigms and a range of supervision strengths. To

guide practitioners, previous work has evaluated performance on various common downstream tasks [18]. A com-

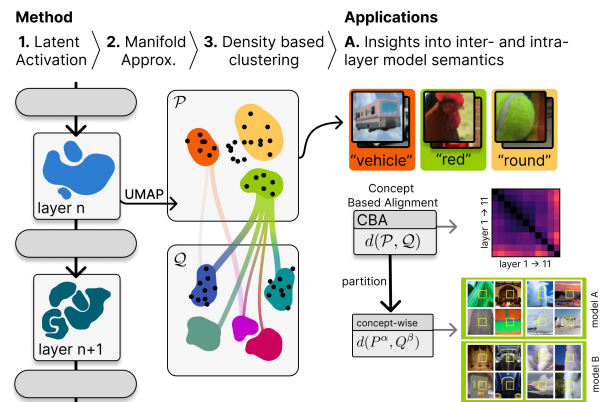


Figure 1. We combine concept discovery with alignment analysis for fine-grained insights into structures within and differences between latent activations. To this end, we investigate latent activations formed by intermediate layers, which according to the manifold hypothesis can be organized in terms of low-dimensional manifolds. We recover manifolds using density-based clustering applied to UMAP embeddings of the latent representations. The discovered structures in latent space do not only allow to characterize a single layer, but also the formation of structures between layers.

plementary view of comparisons within and between models beyond quantitative accuracy is achieved by analyzing patterns in hidden activations and measuring representational alignment between them [34, 40].

When choosing a model for a downstream task, we want to understand how the model solves its pre-training task. Where does the model representation change the most and how? Which concepts, i.e. dominant structures in representation space, are encoded in lower layers vs. upper layers? Where does the model representation change the most and how? How structured are the representations? Does the model encode semantically similar concepts in spatial proximity to each other? How is the representation of model A

different from that of model B across layers? Answering these questions can aid the selection of pre-trained models and the design of fine-tuning strategies through detailed insights into robustness and generalization capabilities. Previous work on alignment, however, only provides a single scalar value to measure alignment between representations at two different layers [38], leaving the questions above largely unanswered. In this paper, we propose a more fine-grained alignment analysis based on concepts that structure the latent representation. To this end, we represent the original activations by concept membership scores that quantify proximity to the discovered concepts. Then, we measure alignment between concept proximity scores of representations and can therefore partition it into the concepts. This gives insights into universal and specific concepts between representations of different layers or models, as well as how a single representation is structured.

To achieve concept-based alignment we need solutions for 1) **concept discovery**, and 2) measuring the **alignment** between concept proximity scores.

Previous work on **concept discovery** ranges from merely identifying neurons or other pre-existing units as concepts [1] to linear directions in feature space [13]. The most general definition so far relies on concepts as multi-dimensional linear subspaces [39]. The common strong assumption among these is the linearity of concept structures, which is challenging to verify and controversial [2, 7]. For concepts that faithfully represent the underlying geometry of the representation, we avoid the linearity assumption and consider concepts as the most general structure they can form, namely as nonlinear manifolds. So far, **alignment** between representations has been measured as the similarity of similarities, e.g. through linear or kernel-based Centred Kernel Alignment (CKA) [25], which results in a single scalar value. Our fine-grained concept-based alignment measure requires a distance measure between concept proximity scores. Here, we choose a generalized Rand index between soft clusterings with pseudo metric properties [23] that we partition into pairwise concept distances.

To summarize, our key idea is the following:

- We combine **concept discovery** with **alignment** analysis to provide insights into which concepts are universal or specific between two representations, and how structured a single representation is.

We make the following methodological contributions to realize concept-based alignment:

- We propose a novel concept definition of concepts as nonlinear manifolds to faithfully capture the geometry of the feature space with concept proximity scores.
- We leverage a generalized Rand index with pseudo-metric properties to measure the alignment between concept proximity scores of two representations and partition it for fine-grained concept alignment.

We complement concept-based alignment analysis of ViTs trained under varying degrees of supervision from fully supervised to self-supervised with additional characteristics of concepts such as their intrinsic dimensionality. We find that representations of ViTs exhibit markedly different structures; specifically, increased supervision correlates with reduced structure in the learned representations. This insight is crucial for understanding the model’s reasoning processes and sheds light on the performance differences observed in quantitative analyses, such as those presented in the recent battle-of-the-backbones study [18]. Code to reproduce our experiments is publicly available at <https://github.com/jvielhaben/NLMCD-ALIGN>.

## 2. Concept Discovery for Representational Alignment

This section is partitioned into three parts: First, we introduce our novel concept definition based on the manifold hypothesis. Then, we describe our methodology for discovering these concepts in latent activations, shown in Fig. 1. Finally, we describe how our concept-based description of hidden representations can be used to measure alignment between representations, identify commonalities and uniqueness between models, and investigate information flow within one model.

### 2.1. Concept definition

**Motivation** According to the manifold hypothesis, which is widely accepted in machine learning, many datasets, including image data that nominally lie in high dimensional space, can be described in terms of a few underlying latent factors and are thus concentrated on a (potentially disconnected) low-dimensional manifold embedded in high-dimensional space [19]. [31] shows how a neural network trained on a toy classification problem solves the task by transforming the topology of the input data, and layerwise reducing the Betti numbers of the class-wise components. We hypothesize that state-of-the-art vision models behave similarly and try to recover the connected components in the hidden representations, which we call *concepts*.

**Definition** We analyze the hidden representation at an intermediate feature layer of a neural network. To this end, we split the model  $f$  into two parts,  $f = g_l \circ h_l$ , where  $h_l$  is the mapping to a hidden feature layer  $l$ . Our definition then relies on hidden representations  $h_l(x_i) \in \mathbb{R}^{N' \times F}$  of input samples  $x_i$  from a set  $S$ .  $N'$  is the number of spatially separable elements in the representation, i.e. the number of tokens in a transformer model or the number of superpixels in a convolutional feature map. We spatially decompose the feature maps  $h(x_i)$  into a set of  $N = N' \cdot |S|$  feature vectors  $\phi \in \mathbb{R}^F$ . Previously, concepts have been mostly defined as linear structures [13, 42]. The most general linear structure

would be affine subspaces, which would already represent an extension compared to the recently considered definition as linear subspaces [39]. In this work, we generalize this idea even one step further and define concepts as manifolds in the  $F$ -dimensional feature space.

**Definition 1** We define a concept  $C^\alpha$ , as a manifold in the  $F$ -dimensional feature space, represented by a point cloud  $\{\phi_j^\alpha\}$  consisting of the feature vectors  $\phi_j$  that lie on the concept manifold with index  $\alpha$ .

**Benefits of concept manifold definition** In the following, we want to compute concept proximity scores by which we measure alignment. Incorrect assumptions about the structure of the concept manifold, e.g., assuming it has no curvature (affine subspaces) or it is spherical and the distance to the manifold can be estimated by the distance to the centroid, directly lead to distorted concept proximity scores and hence to distorted alignment. Later, in a sanity check our definition performs best for measuring representational alignment.

## 2.2. Concept discovery

**Clustering** Having established our definition of concepts as manifolds in feature space, we now turn to the challenge of discovering these concepts through clustering. As stated above, we assume that feature vectors  $\{\phi_i\}$  from a hidden representation are sampled from a set of low-dimensional concept manifolds  $\{C^\alpha\}$ . Recovering these concept manifolds in high-dimensional space ( $F = 768$  in our experiments) is a challenging clustering problem. Therefore, we revert to density-based clustering on a low-dimensional embedding of the data [17, 21]. For this embedding, we utilize UMAP (Uniform Manifold Approximation and Projection) [27], a dimensionality reduction technique that preserves local and some global structure. Given that we have no a priori knowledge about the number of clusters, we employ HDBSCAN (Hierarchical Density-Based Spatial Clustering of Applications with Noise), which can handle clusters of varying densities [4]. HDBSCAN builds a hierarchy of clusters based on density, represented by a condensed tree, and allows for robust handling of noise, making it suitable for the possibly intricate structure of feature representation spaces. While UMAP does not fully preserve density, its ability to maintain the overall structure of the data makes it a valuable preprocessing step before applying HDBSCAN. We use the HDBSCAN implementation from [28].

**Concept proximity scores** We leverage soft clustering with HDBSCAN based on the condensed tree which is roughly a density function over the data points to compute fuzzy cluster membership as described in [28], which we formalize in the appendix for the reader’s convenience. It is

based on the distance to concept anchor points a cluster and an outlier score, both derived from the condensed tree. We now have a fuzzy clustering  $\mathcal{P}_{\{\phi\}} = \{\mathcal{P}(\phi_0), \dots, \mathcal{P}(\phi_N)\}$ , where  $\mathcal{P} \in [0, 1]^n$  holds the concept proximity scores of each concept  $C^\alpha$ . We interpret the concept proximity scores  $P^\alpha(\phi)$  as the probability that a feature vector  $\phi$  belongs to a concept  $P^\alpha$  in clustering  $\mathcal{P}$ . This approach contrasts with previous concept assignment paradigms [13, 39], which often rely on hard clustering, where each feature vector is assigned to a single concept, or linear methods that project onto specific concept directions, limiting the representation to a more rigid framework. In contrast, our soft clustering method allows for nuanced membership scores that reflect the degree of belonging to multiple concepts. In the following, we refer to our concept discovery method as *NLMCD* (non-linear multi-dimensional concept discovery).

## 2.3. Concept-based Representational Alignment

We now address the question of measuring representational alignment based on the concept proximity scores derived from fuzzy clustering.

**Pseudo-metric between fuzzy clusterings** The concepts are at this point characterized by a probabilistic clustering  $\mathcal{P}_{\{\phi\}} = \{\mathcal{P}(\phi_0), \dots, \mathcal{P}(\phi_N)\}$ , where  $\mathcal{P}(\phi_i) = \{P^1(\phi_i), \dots, P^n(\phi_i)\}$ . We want to measure the similarity between two probabilistic clusterings  $\mathcal{P}, \mathcal{Q}$  from two different representations to evaluate how aligned their concepts are. For this purpose, we leverage an extension of the pair-based Rand index generalized to fuzzy clusterings proposed in [23]. The original Rand index counts the number of concordant pairs (either two points are paired or not paired both clusterings) and discordant pairs (two points are paired in one clustering but not in the other). The distance between probabilistic clustering  $\mathcal{P}, \mathcal{Q}$  is based on a generalized degree of concordance that is based on the *distance between two membership vectors*  $d_{ms}(\mathcal{P}(\phi_i), \mathcal{P}(\phi_j))$ :

$$d_{cross}(\mathcal{P}, \mathcal{Q}) = \frac{2}{N(N-1)} \sum_{i,j} |d_{ms}(\mathcal{P}(\phi_i), \mathcal{P}(\phi_j)) - d_{ms}(\mathcal{Q}(\phi_i), \mathcal{Q}(\phi_j))| \quad (1)$$

A commonly used choice for the distance  $d_{ms}$  is  $d_{ms}(\mathcal{P}(\phi_i), \mathcal{P}(\phi_j)) = 1 - \|P(\phi_i) - P(\phi_j)\|_1$  [8]. Finally, we refer to the similarity between two clusterings, derived from the uncovered concepts, as *Concept-Based Alignment* (CBA):

$$CBA = 1 - d_{cross}(\mathcal{P}, \mathcal{Q}) \quad (3)$$

We choose this measure because  $d_{cross}(\mathcal{P}, \mathcal{Q})$  is a pseudo-metric satisfying desirable properties<sup>1</sup> that ease interpreta-

<sup>1</sup> 1) Identity:  $d(x, x) = 0$  for all  $x$ , 2) Symmetry:  $d(x, y) = d(y, x)$  for all  $x, y$ , 3) Triangle Inequality:  $d(x, z) \leq d(x, y) + d(y, z)$  for all  $x, y, z$ .

tion Also, when  $\mathcal{P}, \mathcal{Q}$  are crisp partitions, CBA reduces to the original Rand index.

**Similarity index between clusters** In contrast to conventional measures for representational alignment that yield a single scalar value, our approach provides a more nuanced measure of representational alignment by assessing similarities and differences between clusters. To measure distance between two clusters  $P^\alpha, Q^\beta$  from two clusterings  $\mathcal{P}, \mathcal{Q}$ , we decompose the distance in Eq. 1 into the contribution of single concepts  $P^\alpha, Q^\beta$  and measure the *pairwise similarity between the membership scores* of each feature

$$d_{cross}(P^\alpha, Q^\beta) = \frac{2}{N^2 - N} \sum_{i,j} ||P^\alpha(\phi_i) - P^\alpha(\phi_j)| - |Q^\beta(\phi_i) - Q^\beta(\phi_j)|| \quad (4)$$

Due to the absolute value in Eq. 1, summing over all pairs  $\alpha, \beta$  does not yield the total  $d_{cross}(\mathcal{P}, \mathcal{Q})$ , but by the triangle inequality  $\sum_{\alpha, \beta} d_{cross}(P^\alpha, Q^\beta) \geq d_{cross}(\mathcal{P}, \mathcal{Q})$  the sum is an upper bound for the overall distance between two clusterings.

### 3. Related work

**Concept discovery** Most existing methods model concepts as linear directions [13, 14, 16, 42]. Generalizing this definition, [39] suggest that concepts can be represented more faithfully as multidimensional linear subspaces, which they discover through sparse subspace clustering. While above methods operate unsupervised without concept labels, [6] employ kernel classifier for supervised, nonlinear concept discovery, showing improvement over linear concepts. In the field of *mechanistic interpretability*, many studies aim to enumerate all *features* encoded in the representations of neural networks [3]. This line of work focuses mainly on language models, often identifying linear features using sparse autoencoders [15, 22, 26]. However, [11] find evidence for the existence of multidimensional non-linear features. Unlike these approaches, our main goal in concept discovery is representation summarization for alignment measurement, rather than interpretability or feature enumeration. For this reason, we employ the most general, non-linear concept definition.

**Alignment** Representational alignment measures are categorized, with a particular emphasis on Centered Kernel Alignment (CKA) in [25]. CKA evaluates the similarity of similarities, either linearly or under a non-linear kernel. Similarly, [9] measure alignment through the similarities of binary k-nearest neighbor adjacency matrices, which resembles CKA with a narrow Gaussian kernel. Our method relates to CKA in that it condenses these similarities into clus-

Model	Training Data	Training Task
FS [37]	ImageNet-1k [36]	Fully supervised learning with labeled data for classification task.
CLIP [33]	WebImageText [33]	Contrastive learning between images and text.
DINO [5]	ImageNet-1k	Knowledge distillation enforcing consistency between augmented views of the same image.
MAE [20]	ImageNet-1k	Masked autoencoders to reconstruct missing pixels of input data.

Table 1. Pre-trained models we study with concept-based alignment, which range from fully supervised to text-image contrastive to self-supervised. Sources for the model weights are provided in the appendix.

ters and subsequently measures the similarity between these clusterings.

**Comparison of Vision Models** On the one hand, alignment measures such as CKA have been used to compare the representations of various architectures, including ViTs and ResNets trained on different tasks, together with the analysis of patterns in attention maps [34, 40]. Further, the analysis of attention patterns reveals differences between self-supervised ViTs [32]. On the other hand, downstream performance is analyzed to guide the selection of pre-trained models for transfer learning. Through this, [24] shows that models pre-trained on ImageNet generalize well but when used as feature extractors in transfer learning, i.e. when weights are completely frozen, perform badly in some settings, suggesting that the features of the last layers do not generalize well. An extensive evaluation of the downstream performance of a large selection of vision models on classification, detection, image retrieval, and generalization is available in [18].

## 4. Results

We evaluate concept discovery in Sec. 4.1, check the superiority of our new concept definition over linear baselines for concept alignment analysis in Sec. 4.2, and perform a concept-alignment analysis between four ViTs in Sec. 4.3.

### 4.1. Concept discovery

First, we outline the concept discovery procedure as described in Sec. 2.2 and evaluate the quality of the UMAP embeddings used for HDBSCAN clustering and the clustering itself. For concept discovery and later analysis of representational alignment, we use a random subset of 25 % of the ImageNet train set, stratified samples across all 1000 classes. We study four different ViTs [10] with the same architecture (base, patch size 16, input size 224) but different

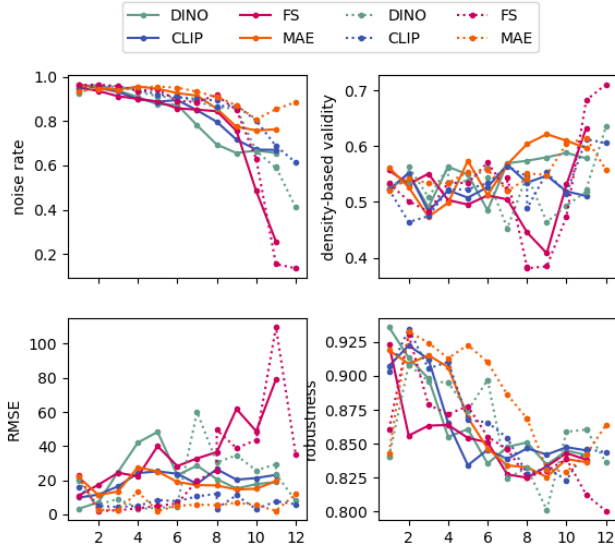


Figure 2. We evaluate the quality of concept discovery. RMSE measures the MSE between the distance matrix of the original and embedded activations and shows how faithfully the UMAP embedding captures the geometry of the representation. DBCV is a density-based clustering validity index that contrasts intra- vs inter-cluster density. The noise rate is the ratio of points classified as noise in HDBSCAN. Robustness is measured between two runs by concept-alignment from Eq. (3). Results are across layers for CLS (dotted) and SEQ (solid) token representations of the models in Tab. 1.

training objectives and training datasets described in Tab. 1. We perform concept discovery separately for the sequence (SEQ) and the CLS token. We extract activations at the last MLP layer of each of the twelve transformer blocks. For the sequence tokens, we average-pool  $4 \times 4$  token and select one of the pooled tokens from the sequence with more weight on the center of the image. For SEQ tokens, we discard the last block as for the considered models only the CLS token in the final layer enters the loss. We evaluate how well the embedding on which we perform the clustering preserves the distances by measuring the mean squared error between the distance matrices in the original representation and its embedding (RMSE). To evaluate the clustering, we compute a density-based validity index (DBCV) [30], which measures intra- vs inter-cluster density. Further, we report the rate of points classified as noise by HDBSCAN. To treat the noise rate and validity index separately, we do not weight the average for the DBCV across clusters by the cluster size as proposed in [30]. Lastly, we evaluate how robust our approach is by measuring the alignment between two runs with different initializations by CBA from Eq. 3. Before discussing the results on embedding and clustering quality (see Fig. 2), we detail the hyperparameter tuning process for UMAP and HDBSCAN. For UMAP, we tune the

minimal distance parameter to enhance local cluster density, acknowledging that a lower minimal distance can increase noise. The number of neighbors parameter controls the local structure captured by the embedding; smaller values capture finer local neighborhoods but may distort the global structure, which is important for subsequent concept alignment analysis. We also experiment with the embedding dimensionality, constrained by practical considerations—the curse of dimensionality renders density clustering in the original high-dimensional representation infeasible, where  $F' = 50$  is the practical limit for the embedding dimensionality. For HDBSCAN, the minimum cluster size parameter is tuned to balance between identifying noise and merging distinct clusters; a too-small value may recognize noise as clusters, while a too-large value could merge distinct clusters. We set the min samples parameter, which controls the algorithm’s conservativeness regarding noise, relatively low due to sampling limitations - some concept manifolds may not be sampled densely enough. We tune all these hyperparameters to maximize the DBCV across models and layers. During hyperparameter tuning, we weight the average DBCV across clusters by their respective sizes to indirectly account for the noise rate. The final hyperparameters used in all subsequent experiments are reported in the appendix. Turning to the results presented in Fig. 2, we observe that RMSE increases slightly across layer for most models. Only for FS there is a strong increase from layer eight onwards, indicating these representations are more difficult to embed and we can trust the clustering on the embedding less which has a high DBCV but low robustness. The density-based validity is medium, but similar across models and SEQ tokens vs. CLS tokens. Given how challenging the clustering task is, we view this result as decent and refer to the convincing qualitative impression of the clusters in Fig. 3 and Fig. 4. Noise rates are rather high but decrease across layers. The high noise may be due to insufficiently dense sampling, i.e. thorough sampling of noisy regions could result in concept clusters. However, the number of input samples is restricted computationally by UMAP and HDBSCAN. Robustness decreases for all models across layers but stagnates at around 0.84 for most models in the late layers. This links back to the trend in RMSE which shows that higher layers are harder to embed. For the qualitative evaluation of our concept discovery method, we construct *concept formation graphs* (CFGs) that depict the flow of token assignments to concepts from one layer to the next as an unweighted, directed graph. Fig. 3 displays the formation of the “apples” concept throughout the layers of the FS model. Note that these graphs may be incomplete, as some nodes might not be detected by the clustering method, illustrating the under-sampling problem described above. Additional examples for other models and the detailed algorithm for CFG construction are provided in the

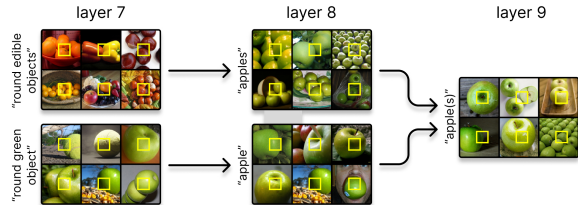


Figure 3. Concept formation graph for the concept “apple(s)” in layer 9 of the FS model. Each concept is represented by six randomly sampled images containing a token assigned to that concept (highlighted in a yellow frame).

appendix.

## 4.2. Sanity checking concept structure for alignment

We use a sanity check to demonstrate how concept-based alignment analysis benefits from concepts defined as non-linear manifolds by comparing against concept alignment based on other definitions and discovery methods. The sanity check is based on the assumption that neighboring representations should be most aligned. We measure the ratio of layers for which a neighboring layer is most aligned under CBA from Eq. (3). We compare NLMCD concepts against one-dimensional linear subspaces discovered by [13], multi-dimensional linear subspaces discovered by MCD [39], and spherical concepts discovered by KMeans clustering [13]. To obtain soft concept membership scores for the linear subspaces, we project the feature vector onto the concept subspace and clip to negative values to 0, as we argue that a feature vector pointing into the opposite direction of a concept signifies the concept not being active. For KMeans concepts, we measure concept proximity by the euclidean distance to the cluster centroid. We also normalize concept membership scores  $P^{\alpha'} = P^{\alpha} / \sum_{\alpha} P^{\alpha}$  as their sum is required to be less bounded by one  $\sum_{\alpha} P^{\alpha} \leq 1$  in Eq. 1. There is no direct way to estimate the number of concepts for PCA, MCD and KMeans, so we use all  $F = 768$  components for PCA for a conservative baseline, and the number of concepts discovered by NLMCD for MCD and KMeans discovery. We present the scores in Tab. 2 for SEQ and CLS token concept alignment. We find that our approach performs best across all models except DINO where PCA achieves the highest score. All other concept frameworks reach NLMCD scores only for single models. For the CLS token, the gap between NLMCD and the other methods is larger than for SEQ token alignment.

## 4.3. Concept Alignment Analysis

We now investigate concept-based alignment described in Sec. 2.3 between representations across layers and models. We structure the analysis into *intra-model* and *inter-model*.

		FS	CLIP	DINO	MAE
SEQ	PCA	0.45	0.90	1.	0.60
	MCD	0.81	0.90	0.81	0.70
	KMeans	<b>0.90</b>	0.90	0.81	<b>1.</b>
	<b>NLMCD</b>	<b>0.90</b>	<b>1.</b>	<b>0.90</b>	<b>1.</b>
CLS	PCA	0.75	0.72	0.50	0.33
	MCD	0.33	0.16	0.16	0.16
	KMeans	0.83	0.91	0.50	0.66
	<b>NLMCD</b>	<b>1.</b>	<b>1.</b>	<b>0.83</b>	<b>0.75</b>

Table 2. Sanity check for concept alignment, showing the percentage of layers where neighboring layers exhibit the highest alignment across various ViT models. We compare the suitability of NLMCD concepts against other methods: one-dimensional linear subspaces (PCA), multi-dimensional linear subspaces (MCD), and spherical concepts (KMeans). NLMCD consistently outperforms other approaches, particularly in CLS token alignment, with the exception of DINO SEQ where PCA achieves the highest score.

Due to limited space, we focus on SEQ representation and defer the CLS representation analysis to the appendix.

**Intra-model representations** We analyze how representations are transformed within one model and how they are structured across layers. To supplement concept-based alignment analysis between representations, we further evaluate alignment with labels from ImageNet-1k and token location and the intrinsic dimensionality of each concept. With this analysis, we answer the questions: 1) Where does the model representation change the most and how? 2) Which concepts are encoded in lower layers vs. upper layers? 3) How structured are the latent representations - does the model encode semantically similar concepts in spatial proximity to each other? opened in the introduction.

**Where does the model representation change the most and how?** First, we focus on the intra-model alignment heatmaps between SEQ representations across layers measured by CBA from Eq. (3) in the upper row of Fig. 4. Interestingly, the transformation process in CLIP, DINO and MAE models is split between the first, i.e., layer one to six, and the second model half, i.e., layer six to eleven. The concept characteristics in Fig. 5 reflect this break and give insight into how the representation is transformed between the break from layers six and seven. The concept count increases rather smoothly across layers for these models, but picks up at layer seven. In contrast, class alignment has a marked increase at this point. For DINO and MAE, the average intrinsic dimensionality of concepts slightly decreases at this point but increases further for CLIP. Lastly, token location alignment also has the most significant decrease at this point. In contrast to the models above, the FS

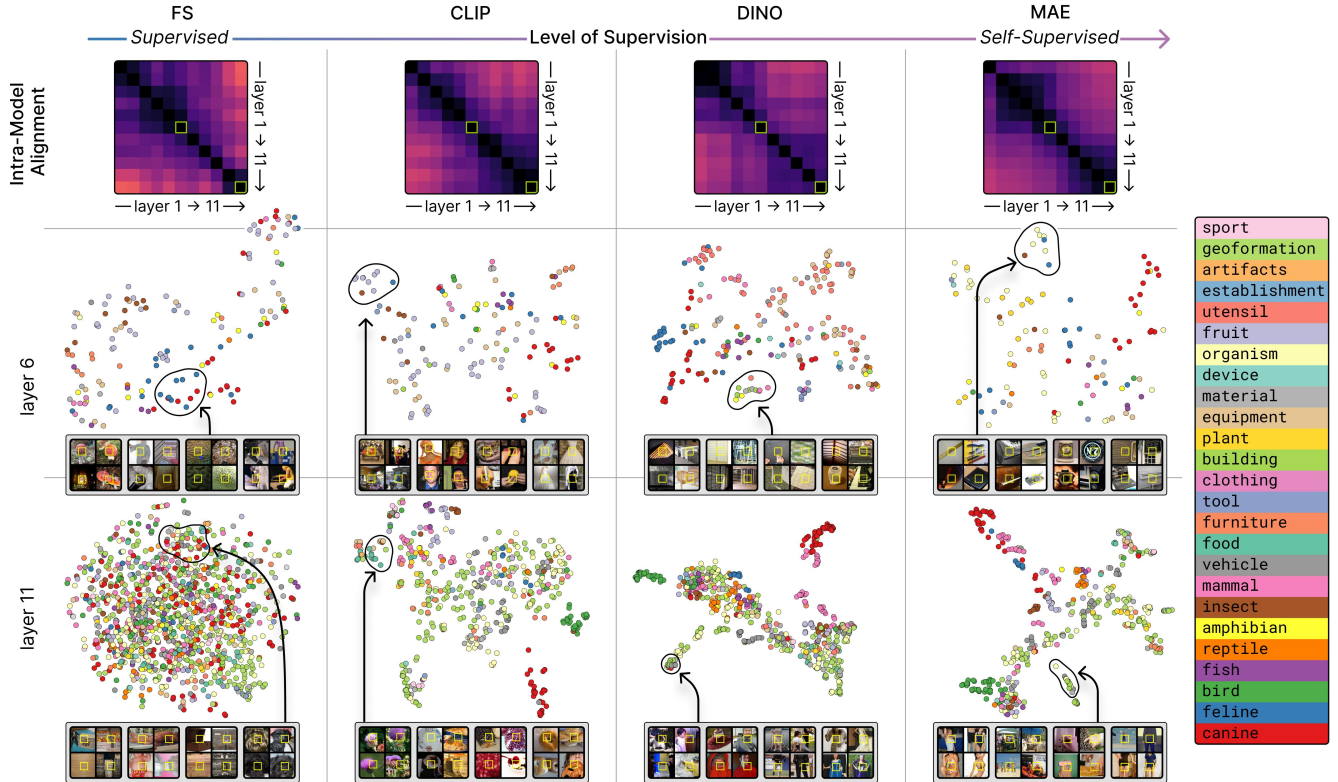


Figure 4. Intra-model relationships based on SEQ representations across layers. In the **upper row**, we show CBA from Eq. (3) to visualize how representations are transformed across layers of the models from Tab. 1 (darker pixels correspond to higher alignment). We observe a nucleation process between layer 9 and 10 in FS and smoother processing split into two major blocks between layer 1-6 and 6-11 in CLIP, DINO and FS. In the **center and bottom row** we zoom into the representations at layer 6 and 11 of each model and partition the scalar CBA alignment into single concepts. We show a UMAP embedding constructed from the pairwise distance of concept measured by  $d_{cross}(P^\alpha, P^\beta)$  from Eq. (4). Each point in this *concept atlas* corresponds to a distinct concept  $P^\alpha$ . To convey their meaning, we show four random input tokens from the members of the concept cluster  $P^\alpha$  marked by a yellow box in the entire image. The higher the level of supervision of ViT training ranging from FS, over CLIP to DINO and MAE, the less semantically organized are the representations at layer 11.

model exhibits a pronounced change rate between nine and ten, resulting in a sudden enhancement in class alignment at layer 10, accompanied by a marked increase in the number of clusters and intrinsic dimensionality. This is reflected in a low alignment between representations in the last two blocks of the FS model and indicates a nucleation process, where concepts begin to separate into distinct classes used for supervised training. This nucleation process has been previously observed in ResNets [9].

**Which concepts are encoded in lower layers vs. upper layers? How structured are the representations?** We now zoom in and partition the representation into single concepts, at layer six just before the block separation in CLIP, DINO, MAE and at layer eleven as the last layer of the second model part. We construct a UMAP embedding based on the distance between concept pairs measured by  $d_{cross}(P^\alpha, P^\beta)$  from Eq. (4). Each point in this *concept at-*

*las* corresponds to a different concept  $P^\alpha$ . To convey their meaning, we show four random input tokens from the members of the concept cluster  $P^\alpha$  (framed by a yellow box). Concept atlases for the representation at layer six and eleven across all models in give a visual impression of how semantically organized the concepts are. To guide the eye, we color-code the concept clusters based on categories derived from the ImageNet-1k labels of the images from which the patches were extracted. We first map these labels to more abstract categories<sup>2</sup> using the WordNet hierarchy [29]. After mapping, we perform a majority vote among all patches in a cluster to assign the category. At layer six, concepts appear structured, but not yet aligned with the WordNet categories. By visual inspection, concepts are less abstract and

<sup>2</sup>The mapping is provided in the appendix. Note that this labeling is only a proxy and may not accurately reflect the actual content of the patches—for instance, a patch might show grass on which an animal stands.

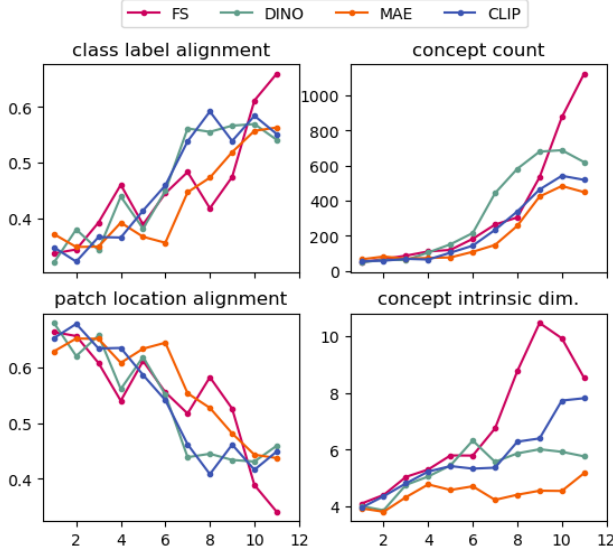


Figure 5. Class label alignment, token location alignment (both based on CBA from Eq. (3)), concept count, and the average intrinsic dimensionality (based on [12]) across concepts supplement the intra-model alignment analysis, by providing insights into how well the model aligns with ImageNet-1k labels, the spatial organization of tokens, and the complexity of the learned concepts as they evolve through the layers.

rather encode structures, shapes and object parts. Representations across ViTs at this layer show a similar level of structuredness. In contrast, at layer eleven, the FS representation is notably less semantically organized than that of the other models. For CLIP, DINO, and MAE we point out how well the canine concepts are separated. To further exemplify, human body parts like neck, shoulder, and legs are grouped together in the representation of DINO and MAE. This alignment requires not only the preservation of local, or intra-cluster distances, but also the maintenance of broader, inter-cluster distances. We conclude that supervised training for the FS model does not enforce this level of semantical organization. In fact, it might make sense to push similar concepts apart in feature space to avoid confusion. However, this likely has negative implications for generalization to other tasks.

**Inter-model relations** We now analyze how the representations between two different models differ and present *CBA* from Eq. (3) between all layers of the models from Tab. 1 in the upper part of Fig. 6. We observe higher alignment between the self-supervised models DINO and MAE than with CLIP and the FS model in the alignment heatmaps. Further, layers of the first are more aligned than those of the second half across all models pairs. We conclude that basic foundational features are learned similarly

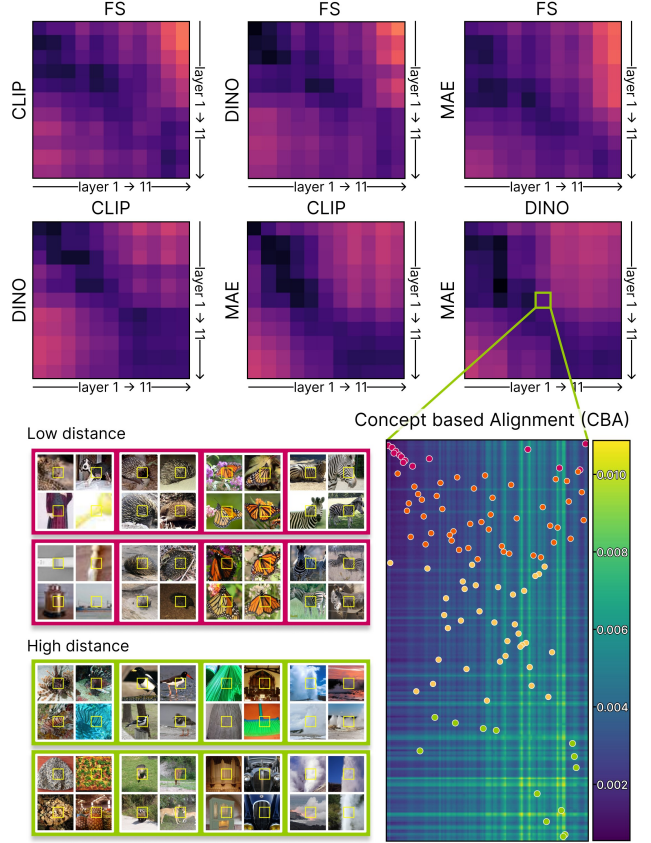


Figure 6. Inter-model relationships based on SEQ representations across layers. In the **upper part**, we show CBA from Eq. (3) to visualize how representations differ between the models in Tab. 1 (darker pixels correspond to higher alignment). In the **lower part** we zoom in into the concept-wise distances  $d_{cross}(P^\alpha, P^\beta)$  from Eq. (4) between the representation of layer six in MAE and DINO. We give examples of universal concepts with low distance and unique ones with high distance from matches of pairs that minimize the total distance.

across models, while later layers diverge as the models specialize to concepts serving their pre-training task.

**How is the representation of model A different from that of model B?** We zoom in into the distance  $d_{cross}(P^\alpha, P^\beta)$  from Eq. (4) between concept pairs from representations of DINO and MAE layer six in the lower part of Fig. 6. We visualize the distance matrix between all concepts. To select specific examples of pairs for inspection, we match concepts via the Hungarian algorithm that minimizes the sum of distances of pairs. From this selection, we show concept pairs with low distance (blurriness, satchel of a hedgehog, zebra stripes) and high distance (complex high-frequency structure, vertically textured structure, fountain and fog-like). Both the universal concepts with low distance and the more specific concepts with



high distance seem to correspond mainly to structure and texture but visual discrepancy is more pronounced for high-distance concepts.

## 5. Conclusion

We propose a novel approach that combines concept discovery with representational alignment analysis in ViTs. With concept-based alignment analysis, we answer the questions raised in the introduction and examine the structuredness in feature spaces of different ViTs, as well as fine details between the concepts of two different models. These insights are not available through traditional scalar alignment measures. Understanding the structured nature of latent spaces can guide practitioners in choosing models that not only perform well on benchmark datasets but also exhibit robust feature representations for downstream tasks. For instance, the nucleation process in FS emphasizes the importance of model structure over mere classification accuracy when selecting a pre-trained model.

**Limitations** The computational scalability of HDBSCAN limits the sampling of feature vectors which makes under-sampled concept regions appear as noise. The limited variability of ImageNet-1k might obfuscate the meaning of a concept, e.g. when a concept represents a color but there are only dog patches of that color.

**Acknowledgments** This work was supported by the European Union’s Horizon Europe research and innovation programme (EU Horizon Europe) as grants [ACHILLES (101189689), TEMA (101093003)]; and the German Research Foundation (DFG) as research unit DeSBI [KI-FOR 5363] (project-id: 459422098).

## References

- [1] David Bau, Bolei Zhou, Aditya Khosla, Aude Oliva, and Antonio Torralba. Network dissection: Quantifying interpretability of deep visual representations. In *Proceedings of the IEEE conference on computer vision and pattern recognition*, pages 6541–6549, 2017. 2
- [2] Leonard Bereska and Stratis Gavves. Mechanistic interpretability for AI safety - a review. *Transactions on Machine Learning Research*, 2024. Survey Certification, Expert Certification. 2
- [3] Trenton Bricken, Adly Templeton, Joshua Batson, Brian Chen, Adam Jermyn, Tom Conerly, Nick Turner, Cem Anil, Carson Denison, Amanda Askell, Robert Lasenby, Yifan Wu, Shauna Kravec, Nicholas Schiefer, Tim Maxwell, Nicholas Joseph, Zac Hatfield-Dodds, Alex Tamkin, Karina Nguyen, Brayden McLean, Josiah E Burke, Tristan Hume, Shan Carter, Tom Henighan, and Christopher Olah. Towards monosemanticity: Decomposing language models with dictionary learning. *Transformer Circuits Thread*, 2023. <https://transformer-circuits.pub/2023/monosemantic-features/index.html>. 4
- [4] Ricardo J. G. B. Campello, Davoud Moulavi, and Jörg Sander. Density-based clustering based on hierarchical density estimates. In *Pacific-Asia Conference on Knowledge Discovery and Data Mining*, 2013. 3
- [5] Mathilde Caron, Hugo Touvron, Ishan Misra, Hervé Jégou, Julien Mairal, Piotr Bojanowski, and Armand Joulin. Emerging properties in self-supervised vision transformers. In *Proceedings of the IEEE/CVF International Conference on Computer Vision (ICCV)*, pages 9650–9660, 2021. 4
- [6] Jonathan Crabbé and Mihaela van der Schaar. Concept activation regions: A generalized framework for concept-based explanations. In *Advances in Neural Information Processing Systems*, pages 2590–2607. Curran Associates, Inc., 2022. 4
- [7] Róbert Csordás, Christopher Potts, Christopher D Manning, and Atticus Geiger. Recurrent neural networks learn to store and generate sequences using non-linear representations. In *The 7th BlackboxNLP Workshop*, 2024. 2
- [8] Ryan DeWolfe and Jeffery L. Andrews. Random models for fuzzy clustering similarity measures. *ArXiv*, abs/2312.10270, 2023. 3
- [9] Diego Doimo, Aldo Glielmo, Alessio Ansuini, and Alessandro Laio. Hierarchical nucleation in deep neural networks. In *Proceedings of the 34th International Conference on Neural Information Processing Systems*, pages 7526–7536, Red Hook, NY, USA, 2020. Curran Associates Inc. 4, 7
- [10] Alexey Dosovitskiy, Lucas Beyer, Alexander Kolesnikov, Dirk Weissenborn, Xiaohua Zhai, Thomas Unterthiner, Mostafa Dehghani, Matthias Minderer, Georg Heigold, Sylvain Gelly, Jakob Uszkoreit, and Neil Houlsby. An image is worth 16x16 words: Transformers for image recognition at scale. In *International Conference on Learning Representations*, 2021. 1, 4
- [11] Joshua Engels, Isaac Liao, Eric J. Michaud, Wes Gurnee, and Max Tegmark. Not all language model features are linear. *ArXiv*, abs/2405.14860, 2024. 4
- [12] Elena Facco, Maria d’Errico, Alex Rodriguez, and Alessandro Laio. Estimating the intrinsic dimension of datasets by a minimal neighborhood information. *Scientific Reports*, 7(1): 12140, 2017. 8, 16
- [13] Thomas Fel, Victor Boutin, Louis Béthune, Remi Cadene, Mazda Moayeri, Léo Andéol, Mathieu Chalvidal, and Thomas Serre. A holistic approach to unifying automatic concept extraction and concept importance estimation. In *Advances in Neural Information Processing Systems*, pages 54805–54818. Curran Associates, Inc., 2023. 2, 3, 4, 6
- [14] Thomas Fel, Agustin Picard, Louis Béthune, Thibaut Boissin, David Vigouroux, Julien Colin, Rémi Cadène, and Thomas Serre. Craft: Concept recursive activation factorization for explainability. In *Proceedings of the IEEE/CVF Conference on Computer Vision and Pattern Recognition (CVPR)*, pages 2711–2721, 2023. 4
- [15] Leo Gao, Tom Dupré la Tour, Henk Tillman, Gabriel Goh, Rajan Troll, Alec Radford, Ilya Sutskever, Jan Leike, and Jeffrey Wu. Scaling and evaluating sparse autoencoders, 2024. 4

- [16] Amirata Ghorbani, James Wexler, James Y Zou, and Been Kim. Towards automatic concept-based explanations. In *Advances in Neural Information Processing Systems*. Curran Associates, Inc., 2019. 4
- [17] Alvina Goh and Rene Vidal. Clustering and dimensionality reduction on Riemannian manifolds. In *2008 IEEE Conference on Computer Vision and Pattern Recognition*, pages 1–7, 2008. ISSN: 1063-6919. 3
- [18] Micah Goldblum, Hossein Souri, Renkun Ni, Manli Shu, Viraj Prabhu, Gowthami Somepalli, Prithvijit Chattopadhyay, Mark Ibrahim, Adrien Bardes, Judy Hoffman, Ramalingam Chellappa, Andrew Gordon Wilson, and Tom Goldstein. Battle of the backbones: A large-scale comparison of pretrained models across computer vision tasks. *ArXiv*, abs/2310.19909, 2023. 1, 2, 4
- [19] Ian Goodfellow, Yoshua Bengio, and Aaron Courville. *Deep Learning*. MIT Press, 2016. <http://www.deeplearningbook.org>. 2
- [20] Kaiming He, Xinlei Chen, Saining Xie, Yanghao Li, Piotr Dollár, and Ross Girshick. Masked autoencoders are scalable vision learners. In *Proceedings of the IEEE/CVF Conference on Computer Vision and Pattern Recognition (CVPR)*, pages 16000–16009, 2022. 4
- [21] Moritz Herrmann, Daniyal Kazempour, Fabian Scheipl, and Peer Kröger. Enhancing cluster analysis via topological manifold learning. *Data Mining and Knowledge Discovery*, 2023. 3
- [22] Robert Huben, Hoagy Cunningham, Logan Riggs Smith, Aidan Ewart, and Lee Sharkey. Sparse autoencoders find highly interpretable features in language models. In *The Twelfth International Conference on Learning Representations*, 2024. 4
- [23] Eyke Hullermeier, Maria Rifqi, Sascha Henzgen, and Robin Senge. Comparing fuzzy partitions: A generalization of the rand index and related measures. *IEEE Transactions on Fuzzy Systems*, 20(3):546–556, 2012. 2, 3
- [24] Simon Kornblith, Jonathon Shlens, and Quoc V. Le. Do better imagenet models transfer better? *2019 IEEE/CVF Conference on Computer Vision and Pattern Recognition (CVPR)*, pages 2656–2666, 2018. 4
- [25] Simon Kornblith, Mohammad Norouzi, Honglak Lee, and Geoffrey Hinton. Similarity of neural network representations revisited. In *International conference on machine learning*, pages 3519–3529. PMLR, 2019. 2, 4
- [26] Samuel Marks, Can Rager, Eric J. Michaud, Yonatan Belinkov, David Bau, and Aaron Mueller. Sparse feature circuits: Discovering and editing interpretable causal graphs in language models, 2024. 4
- [27] Leland McInnes and John Healy. Umap: Uniform manifold approximation and projection for dimension reduction. *ArXiv*, abs/1802.03426, 2018. 3
- [28] Leland McInnes, John Healy, and Steve Astels. hdbscan: Hierarchical density based clustering. *The Journal of Open Source Software*, 2(11), 2017. 3, 11
- [29] George A. Miller. Wordnet: a lexical database for english. *Commun. ACM*, 38(11):39–41, 1995. 7
- [30] Davoud Moulavi, Pablo A. Jaskowiak, Ricardo J. G. B. Campello, Arthur Zimek, and Jörg Sander. Density-based clustering validation. In *SDM*, 2014. 5
- [31] Gregory Naitzat, Andrey Zhitnikov, and Lek-Heng Lim. Topology of deep neural networks. *The Journal of Machine Learning Research*, 21(1):184:7503–184:7542, 2020. 2
- [32] Namuk Park, Wonjae Kim, Byeongho Heo, Taekyung Kim, and Sangdoon Yun. What do self-supervised vision transformers learn? *ArXiv*, abs/2305.00729, 2023. 4
- [33] Alec Radford, Jong Wook Kim, Chris Hallacy, Aditya Ramesh, Gabriel Goh, Sandhini Agarwal, Girish Sastry, Amanda Askell, Pamela Mishkin, Jack Clark, Gretchen Krueger, and Ilya Sutskever. Learning transferable visual models from natural language supervision. In *Proceedings of the 38th International Conference on Machine Learning*, pages 8748–8763. PMLR, 2021. 4
- [34] Maithra Raghu, Thomas Unterthiner, Simon Kornblith, Chiyuan Zhang, and Alexey Dosovitskiy. Do vision transformers see like convolutional neural networks? In *Neural Information Processing Systems*, 2021. 1, 4
- [35] Sebastian Raschka, Joshua Patterson, and Corey Nolet. Machine learning in python: Main developments and technology trends in data science, machine learning, and artificial intelligence. *arXiv preprint arXiv:2002.04803*, 2020. 12
- [36] Olga Russakovsky, Jia Deng, Hao Su, Jonathan Krause, Sanjeev Satheesh, Sean Ma, Zhiheng Huang, Andrej Karpathy, Aditya Khosla, Michael Bernstein, Alexander C. Berg, and Li Fei-Fei. Imagenet large scale visual recognition challenge. *International Journal of Computer Vision*, 115(3):211–252, 2015. 4
- [37] Andreas Peter Steiner, Alexander Kolesnikov, Xiaohua Zhai, Ross Wightman, Jakob Uszkoreit, and Lucas Beyer. How to train your vit? data, augmentation, and regularization in vision transformers. *Transactions on Machine Learning Research*, 2022. 4
- [38] Ilija Sucholutsky, Lukas Muttenthaler, Adrian Weller, Andi Peng, Andreea Bobu, Been Kim, Bradley C. Love, Erin Grant, Jascha Achterberg, Joshua B. Tenenbaum, Katherine M. Collins, Katherine L. Hermann, Kerem Oktar, Klaus Greff, Martin N. Hebart, Nori Jacoby, Qiuyi Zhang, Raja Marjeh, Robert Geirhos, Sherol Chen, Simon Kornblith, Sunayana Rane, Talia Konkle, Thomas P. O’Connell, Thomas Unterthiner, Andrew Kyle Lampinen, Klaus-Robert Muller, Mariya Toneva, and Thomas L. Griffiths. Getting aligned on representational alignment. *ArXiv*, abs/2310.13018, 2023. 2
- [39] Johanna Vielhaben, Stefan Bluecher, and Nils Strodthoff. Multi-dimensional concept discovery (MCD): A unifying framework with completeness guarantees. *Transactions on Machine Learning Research*, 2023. 2, 3, 4, 6
- [40] Matthew Walmer, Saksham Suri, Kamal Gupta, and Abhinav Shrivastava. Teaching matters: Investigating the role of supervision in vision transformers. *2023 IEEE/CVF Conference on Computer Vision and Pattern Recognition (CVPR)*, pages 7486–7496, 2022. 1, 4
- [41] Ross Wightman. Pytorch image models. <https://github.com/rwightman/pytorch-image-models>, 2019. 12

[42] Ruihan Zhang, Prashan Madumal, Tim Miller, Krista A. Ehinger, and Benjamin I. P. Rubinstein. Invertible concept-based explanations for cnn models with non-negative concept activation vectors. *Proceedings of the AAAI Conference on Artificial Intelligence*, 35(13):11682–11690, 2021. 2, 4

## A. HDBSCAN

After concept discovery with HDBSCAN, we compute concept proximity scores  $\mathcal{P}_{\{\phi\}} = \{\mathcal{P}(\phi_0), \dots, \mathcal{P}(\phi_N)\}$ , where  $\mathcal{P} \in [0, 1]^n$  holds the concept proximity scores  $P^\alpha$  of each concept  $C^\alpha$ . These rely on the implementation of soft clustering with HDBSCAN from [28], which we formalize here for the reader’s convenience.

**Clustering** HDBSCAN first transforms the feature space using a density-informed metric called *mutual reachability distance*

$$\text{MRD}(\phi_i, \phi_j) = \max(\text{coreDistance}_k(\phi_i), \text{coreDistance}_k(\phi_j), d(\phi_i, \phi_j)) \quad (5)$$

where  $\text{coreDistance}_k(\phi)$  is the distance between a point  $\phi$  and its  $k$ -nearest neighbor. Based on the mutual reachability distance between all pairs, a minimum spanning tree is constructed that connects all points and minimizes the sum of the edges weighted by MRD. From this, a hierarchical tree is constructed via robust single linkage clustering. The hierarchical tree is condensed by eliminating insignificant clusters and simplifying the hierarchy. This is achieved by selecting a range of *persistence* values  $\lambda$ , which are the inverses of the mutual reachability distances ( $\lambda = 1/\text{MRD}$ ). Clusters that persist over significant ranges of  $\lambda$ , i.e. they are stable across multiple density levels, are retained, while clusters that exist only over narrow ranges of  $\lambda$  are considered noise and pruned from the tree. The result is a condensed tree that focuses on the most significant clusters. Finally clusters are extracted from the condensed tree either based on their stability across different density levels or simply the leaf nodes are identified as clusters.

**Soft clustering with HDBSCAN** The soft cluster membership scores combine a distance-based membership with an outlier score.

For the **distance-based membership** to cluster  $C^\alpha$ , first  $k$  exemplar points  $\{\phi_i^\alpha\}$ ,  $i \in [1, k]$ , are extracted. A single centroid is not enough to characterize a cluster as its shape can be arbitrary. The exemplar points are the points within the leaf nodes beneath cluster  $C^\alpha$  with maximum persistence  $\lambda$  in the condensed tree, i.e. the densest points where the cluster persists.

Then, the distance membership score between a point  $\phi$  and a cluster  $C^\alpha$  is the inverse minimum distance across the exemplar points  $\{\phi_i^\alpha\}$ ,

$$M^\alpha(\phi)_{\text{dist}} = \frac{[\min_i(d(\phi, \phi_i^\alpha))]^{-1}}{\sum_\beta [\min_j(d(\phi, \phi_j^\beta))]^{-1}}, \quad (6)$$

normalized across all clusters.

The **outlier-based membership** compares a point’s membership persistence to the total persistence of a cluster:

$$M^\alpha(\phi)_{\text{membership}} = \frac{\lambda_{\phi \rightarrow C^\alpha} - \lambda_{\text{birth}}^{C^\alpha}}{\lambda_{\text{max}}^{C^\alpha} - \lambda_{\text{birth}}^{C^\alpha}}. \quad (7)$$

Here,  $\lambda_{\text{birth}}^{C^\alpha}$  is the persistence value at which cluster  $C^\alpha$  first appears, i.e. its birth point in the condensed tree and  $\lambda_{\phi \rightarrow C^\alpha}$  is the persistence value at which point  $\phi$  would join cluster  $C^\alpha$ .

Finally, distance and outlier-based membership are combined with stronger emphasis on outlier-based membership,

$$M^\alpha(\phi) = (M^\alpha(\phi)_{\text{dist}})^{1/2} \cdot (M^\alpha(\phi)_{\text{membership}})^2, \quad (8)$$

and normalized  $M_{\text{norm}}^\alpha(\phi) = M^\alpha(\phi) / \sum_\beta M^\beta(\phi)$ .

This membership score  $M_{\text{norm}}^\alpha(\phi)$  can be interpreted as the probability that a point  $\phi$  belongs to cluster  $C^\alpha$ , given that the point belongs to some cluster,

$$M_{\text{norm}}^\alpha(\phi) \equiv P(\phi \in C^\alpha \mid \exists \beta : \phi \in C^\beta). \quad (9)$$

We want to compute the joint probability  $P(\phi \in C^\alpha)$ , which includes the probability that  $\phi$  may be noise,

$$P(\phi \in C^\alpha) = P(\phi \in C^\alpha \mid \exists \beta : \phi \in C^\beta) P(\exists \beta : \phi \in C^\beta). \quad (10)$$

Here,  $P(\exists \beta : \phi \in C^\beta)$  is the probability that  $\phi$  belongs to some cluster. To estimate  $P(\exists \beta : \phi \in C^\beta)$ , the  $\lambda$  value at which  $\phi$  would join the nearest cluster is compared to the maximum  $\lambda$  value of that cluster,

$$P(\exists \beta : \phi \in C^\beta) = \frac{\lambda_{\phi \rightarrow C^\alpha}}{\lambda_{\text{max}}^{C^\alpha}}, \quad (11)$$

where  $\lambda_{\phi \rightarrow C^\alpha}$  is the persistence value at which point  $\phi$  would join its nearest cluster  $C^\alpha$  and  $\lambda_{\text{max}}^{C^\alpha}$  is the maximum  $\lambda$  value of cluster  $C^\alpha$ . Thus, the final probability, that point  $\phi$  belongs to cluster  $C^\alpha$  is,

$$P^\alpha(\phi) = \frac{\lambda_{\phi \rightarrow C^\alpha}}{\lambda_{\text{max}}^{C^\alpha}} \cdot M_{\text{norm}}^\alpha(\phi). \quad (12)$$

## B. Details on experimental setup

Here, we provide further details on the experiments.

**ViT sources** We list the URL of each Vision Transformer provided by the timm library [41]:

- FS: [https://huggingface.co/timm/vit\\_base\\_patch16\\_224.augreg\\_in1k](https://huggingface.co/timm/vit_base_patch16_224.augreg_in1k)
- CLIP: [https://huggingface.co/timm/vit\\_base\\_patch16\\_clip\\_224.openai](https://huggingface.co/timm/vit_base_patch16_clip_224.openai)
- DINO: [https://huggingface.co/timm/vit\\_base\\_patch16\\_224.dino](https://huggingface.co/timm/vit_base_patch16_224.dino)
- MAE: [https://huggingface.co/timm/vit\\_base\\_patch16\\_224.mae](https://huggingface.co/timm/vit_base_patch16_224.mae)

**Hyperparameters for UMAP and HDBSCAN** We tune hyperparameters of UMAP and HDBSCAN such that the density-based validity index DBCV is maximized across models and layers. Here, for DBCV, the average across clusters is weighted by their respective size such that the noise rate is indirectly included. We re-iterate the effect of the most influential hyperparameters that we tune and state the final value we used:

- **Minimal distance in UMAP:** a low minimal distance in UMAP enhances local cluster density but may also increase noise. We use a value of 0.01 in all experiments.
- **Number of neighbours in UMAP:** the number of neighbors controls the local structure, the smaller the finer it captures local neighborhoods but distorts global structure which is important for concept alignment analysis later. We use a value of 30 in all experiments.
- **Embedding dimensionality in UMAP:** We use the practical limit for HDBSCAN of  $F' = 50$  in all experiments.
- **Minimum cluster size in HDBSCAN:** a too small minimum cluster size may identify noise as a cluster, whereas, when too large, distinct clusters will merge. We use a value of 50 in all experiments.
- **Min samples in HDBSCAN:** controls how conservative the algorithm is about noise. We need this to be rather low because of sampling limitations which means that most likely some concept manifolds are not sampled densely enough. We use a value of 20 in all experiments.

Additionally, we assume that clusters are rather uniform in size and select the leaf nodes in the HDBSCAN hierarchical condensed tree as clusters. Sampling one pooled SEQ token (we average-pool over  $4 \times 4$  tokens) or one CLS token from each representation of images within a 25% subset of the ImageNet1-1k train set results in 315.770 feature vectors  $\phi_i$  for clustering. We use the cuML [35] versions of HDBSCAN and UMAP for computation on the GPU.

**Cluster label in Concept Atlas** To assign a label from the WordNet Hierarchy to each concept cluster, we first assign the ImageNet-1k label of the image from which a token is extracted to its representation feature vector  $\phi_i$ . Then we map this to a label higher in the WordNet hierarchy by the

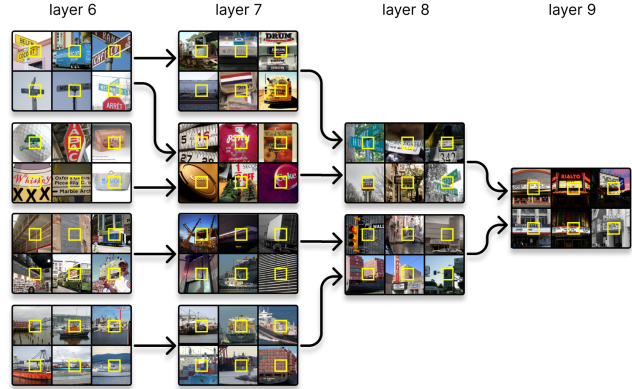


Figure 7. Concept formation graph for a concept in layer 9 of DINO. Each concept is represented by six randomly sampled images containing a token assigned to that concept (highlighted in a yellow frame).

mapping in Tab. 3. We then assign the most frequent label among the cluster members  $\{\phi_j^\alpha\}$  to the cluster  $C^\alpha$ .

**Computation of alignment** Our concept-based alignment measure CBA is based on pairs of feature vectors  $(\phi_i, \phi_j)$ . To reduce run-time, we sub-sample 20% of the 315.770 feature vectors before computing CBA.

## C. Concept Formation Graphs

The algorithm for construction of a concept formation graph is defined as follows:

1. **Token assignment:** We begin by assigning each token in each layer to either one or more concepts or marking it as noise. Soft assignments are thresholded.
2. **Transition matrix calculation:** Next, we compute transition matrices for each pair of consecutive layers,  $(n, n + 1)$ . Each matrix entry represents the count of tokens transitioning from a concept in layer  $n$  to a concept in layer  $n + 1$ .
3. **Recursive graph construction:** The CFG for a target node is then constructed recursively. Starting from the target node, we add all predecessor concepts whose “contribution” (the proportion of incoming transitions) surpasses a specified threshold. The resulting CFG is a binary, unidirectional graph in which nodes representing noise are excluded.

Figs. 7 to 9 illustrate additional exemplary CFGs for CLIP and DINO.

## D. Concept alignment analysis

### D.1. CLS representations

We investigate concept-based alignment within and across models based on the CLS token representations analogous

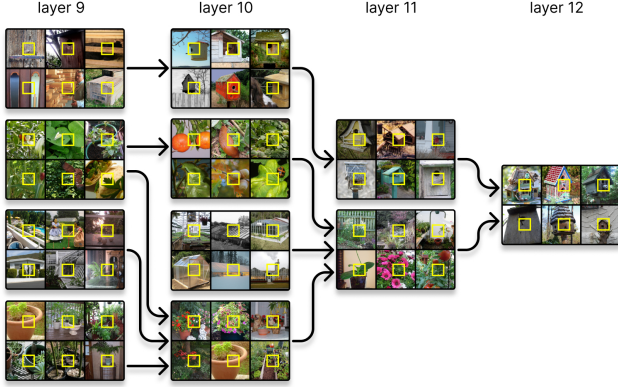


Figure 8. Concept formation graph for a concept in layer 12 of CLIP. Each concept is represented by six randomly sampled images containing a token assigned to that concept (highlighted in a yellow frame).

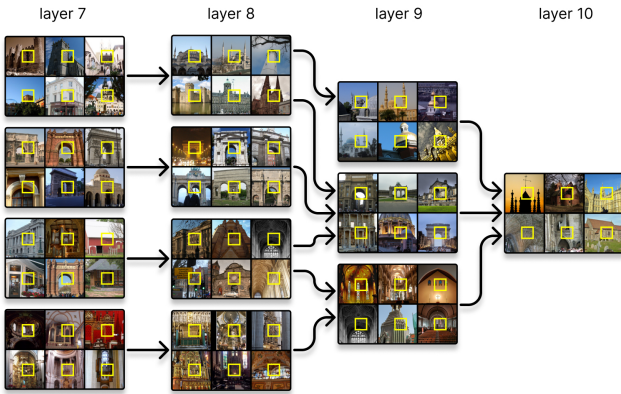


Figure 9. Concept formation graph for a concept in layer 10 of CLIP. Each concept is represented by six randomly sampled images containing a token assigned to that concept (highlighted in a yellow frame).

to the SEQ token analysis in the main paper.

**Intra-model alignment** First, we focus on the intra-model alignment heatmaps between CLS representations across layers measured by CBA in the upper row of Fig. 10 and compare it to the same analysis between SEQ representations shown in the main paper. For the CLS representations of the FS model we see a very similar pattern as for the SEQ representations. Also for CLIP and MAE, the CLS intra-model alignment mirrors that of the SEQ representations; however, the first two and one blocks, respectively, show significantly lower alignment than in the SEQ tokens. This is reasonable since the model might not use these for processing information in the early blocks. Interestingly, for DINO, the CLS token alignment across layers is significantly lower than the SEQ token alignment. Class label alignment, intrinsic dimensionality of concept clusters and

concept count for the CLS representations in Fig. 11 are also similar to the SEQ results except for DINO. Here, DINO CLS concepts exhibit a notable difference to DINO SEQ concepts: the concept count, class alignment, and intrinsic dimensionality increase sharply between blocks 9 and 10 for the CLS representation but not for the SEQ representation. Lastly, the structure of the concept atlases in the lower part of Fig. 10 differs the most from the structure of the SEQ concept atlases for DINO, where CLS concepts at layer 11 are less semantically organized than SEQ concepts. These observations suggest that the differences in how CLS and SEQ tokens represent and abstract information are most pronounced in DINO among the models.

**Inter-model alignment** Second, we analyze how the CLS representations between two different models differ and present CBA alignment between all layers and model in the upper part of Fig. 12. Like for the SEQ representations, CLS representations at layers of the first are more aligned than those of the second half across all models pairs, suggesting that basic foundational features are learned similarly across models, while later layers diverge as the models specialize to concepts serving their pre-training task. However, the overall alignment between models is weaker for CLS representations than for SEQ, also in low layers. Next, we zoom in into the distance  $d_{cross}(P^\alpha, P^\beta)$  between concept pairs from CLS representations of DINO layer 3 and MAE layer four in the lower part of Fig. 12. We visualize the distance matrix between all concepts and inspect pairs of concepts matched via the Hungarian algorithm. Most of the concepts in the pairs seem to correspond to the color composition of the images. Visual discrepancy is more pronounced for high-distance concepts than for the other pairs with lower distance.

## D.2. Additional results for SEQ representations

**Intra-model** To give a more detailed view of the organization of concepts across the layers of one model, we select the DINO model and show the respective concept atlases at layer one, six and eleven in Fig. 13, Fig. 14, and Fig. 15, respectively. To give an overview of the structure within a concept atlas, we group the concepts in the UMAP embedding via KMeans and show four random concepts for each group. In layer one, many concepts correspond to color, in layer six, they represent mostly textures, and in layer eleven they correspond to abstract concepts. Mostly, concepts within a group are of similar nature.

**Inter-model** In the main paper, we show fine-grained inter-model concept distances between DINO and MAE at layer six in the center of the both models. Here, we add fine-grained concept distance analysis in the first and last part of the models in Fig. 16 and Fig. 17. We show the full

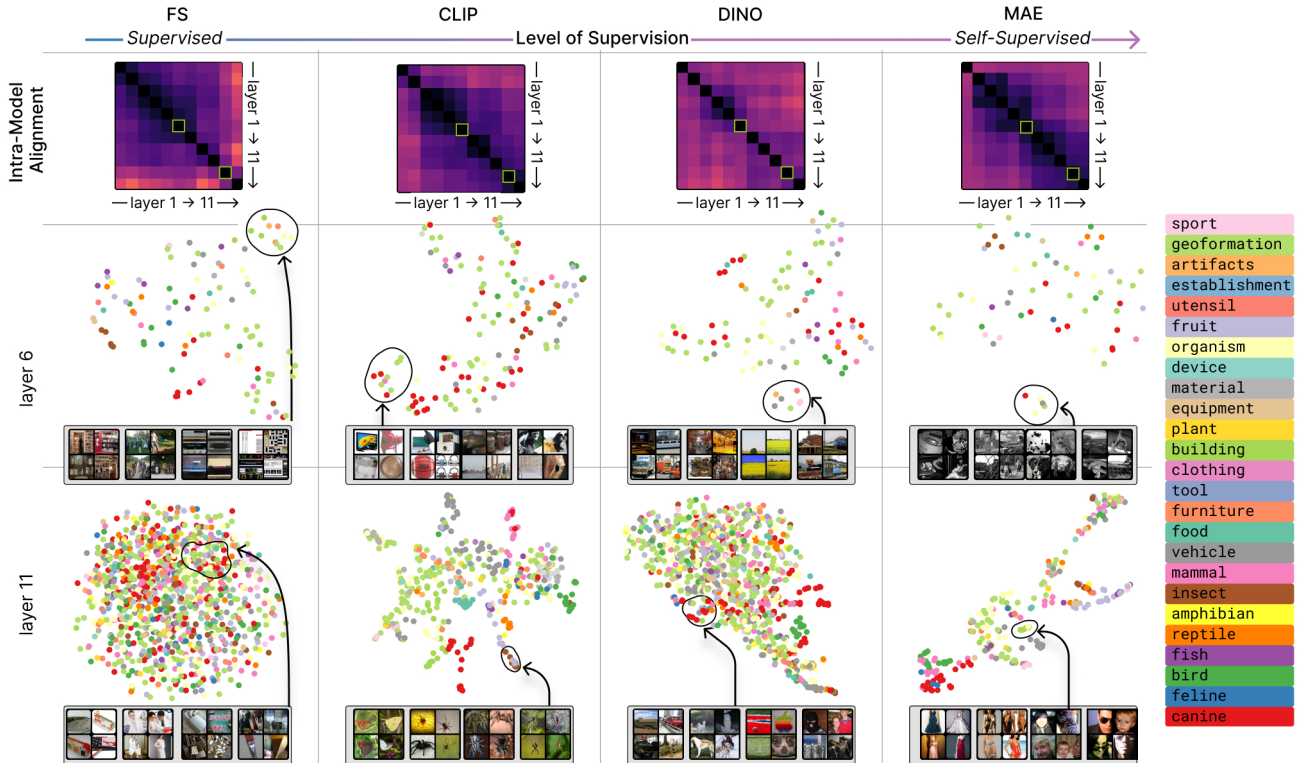


Figure 10. Intra-model relationships based on CLS representations across layers. In the **upper row**, we show CBA to visualize how representations are transformed across layers of the models (darker pixels correspond to higher alignment). In the **center and bottom row** we zoom into the representations at layer 6 and 11 of each model and partition the scalar CBA alignment into single concepts. We show a UMAP embedding constructed from the pairwise distance of concept measured by  $d_{cross}(P^\alpha, P^\beta)$ . Each point in this *concept atlas* corresponds to a distinct concept  $P^\alpha$ . To convey their meaning, we show four random input tokens from the members of the concept cluster  $C^\alpha$  marked by a yellow box in the entire image.

pairwise distance matrix as well as how distances between matched pairs are distributed. We partition the pairs into four regimes of distances with low, medium-low, medium-high, and high distance. The concept pairs between MAE layer 3 and DINO layer 2 seem to correspond mostly to edge detectors or abstract patterns. Among the low and medium-low distance pairs are grid vs. stripes (second low-distance concept pair) and diagonal edge detectors (second medium-low distance concept pair). The common nature of the medium-high to high-distance pairs is hard to interpret but pairs include warm vs. bright light (first medium-high distance concept pair), and blurriness (third high-distance concept pair). The limitation of visualizing low-level concepts through ImageNet-1k images, as described in the main paper, becomes apparent here. In contrast, the matched concept pairs between MAE and DINO layer 10 are easier to interpret - e.g. owl face or flame.

Category	ImageNet-1k class
amphibian	European fire salamander axolotl bullfrog common newt eft spotted salamander tailed frog tree frog
artifacts	Afghan hound Band Aid Dutch oven Petri dish abacus ashan backpack ballpoint bannister barrel bath towel bathtub beacon beaker beer bottle beer glass bell cote binder birdhouse book jacket bottlecap brass breakwater breastplate broom bucket cannon carousel carton cassette chain mail chainlink fence chiffonier cleaver cliff dwelling cloak clog cocktail shaker coffee mug comic book cowboy boot crate crib crutch cuirass cup diaper dishwasher dock envelope espresso maker face powder fig fire screen flagpole fountain fountain pen gasmask goblet grasshopper grille grocery store guillotine hair spray hand blower holster honeycomb iron "jack-o-lantern" joystick ladle lampshade lens cap library lipstick lotion mailbox manhole cover mask matchstick maze measuring cup megalith menu microwave minibus mixing bowl mobile home mortar mortarboard mosquito net mountain tent muzzle necklace obelisk packet paddle patio pedestal pencil box pencil sharpener perfume pickelhaube picket fence pier piggy bank pill bottle pillow pitcher plastic bag plate rack pole pop bottle pot prayer rug purse quill quilt racket radio rain barrel refrigerator rotisserie rubber eraser running shoe safe saltshaker scabbard school bus schooner scoreboard shield shoji shopping basket shower curtain ski mask sleeping bag sliding door soap dispenser soup bowl space bar spotlight steel arch bridge stone wall stove street sign stretcher sunscreen suspension bridge swab swing teddy television thatch theater curtain thimble tile roof totem pole traffic light tray triumphal arch trolleybus tub turnstile umbrella vacuum vase viaduct waffle iron washbasin washer water bottle water jug water tower web site whiskey jug window screen window shade wine bottle worm fence wreck yurt
bird	African grey American coot American egret European gallinule albatross bald eagle bee eater bittern black grouse black stork black swan brambling bulbul bustard chickadee cock coucal crane dowitcher drake flamingo goldfinch goose great grey owl hen hornbill house finch hummingbird indigo bunting jacamar jay junco king penguin kite limpkin little blue heron lorikeet macaw magpie ostrich oystercatcher partridge pelican prairie chicken ptarmigan quail red-backed sandpiper red-breasted merganser redshank robin ruddy turnstone ruffed grouse spoonbill sulphur-crested cockatoo toucan vulture water ouzel white stork
building	apiary barn boathouse castle church cinema greenhouse home theater monastery mosque palace planetarium prison restaurant stage stupa vault
canine	African hunting dog Airedale American Staffordshire terrier Appenzeller Arctic fox Australian terrier Bedlington terrier Bernese mountain dog Blenheim spaniel Border collie Border terrier Boston bull Bouvier des Flandres Brabancon griffon Brittany spaniel Cardigan Chesapeake Bay retriever Chihuahua Dandie Dimont Doberman English foxhound English setter English springer EntleBucher Eskimo dog French bulldog German short-haired pointer Gordon setter Great Dane Great Pyrenees Greater Swiss Mountain dog Ibizan hound Irish setter Irish terrier Irish water spaniel Irish wolfhound Italian greyhound Japanese spaniel Kerry blue terrier Labrador retriever Lakeland terrier Leonberg Lhasa Maltese dog Mexican hairless Newfoundland Norfolk terrier Norwegian elkhound Norwich terrier Pekinese Pembroke Pomeranian Rhodesian ridgeback Rottweiler Saint Bernard Saluki Samoyed Scotch terrier Scottish deerhound Sealham terrier Shetland sheepdog Shih-Tzu Siberian husky Staffordshire bullterrier Sussex spaniel Tibetan mastiff Tibetan terrier Walker hound Weimaraner Welsh springer spaniel West Highland white terrier Yorkshire terrier affenpinscher basenji basset beagle black-and-tan coonhound bloodhound blue tick borzoi briard bull mastiff cairn chow choker cocker spaniel collie coyote curly-coated retriever dalmatian dhole dingo flat-coated retriever giant schnauzer golden retriever grey fox groenendael hyena keeshond kelpie kit fox komondor kuvasz malamute malinois miniature pinscher miniature poodle miniature schnauzer otterhound papillon pug red fox red wolf redbone schipperke silky terrier soft-coated wheaten terrier standard poodle standard schnauzer timber wolf toy poodle toy terrier vizsla whippet white wolf wire-haired fox terrier
clothing	Christmas stocking Loafer Old English sheepdog Windsor tie abaya academic gown apron bathing cap bearskin bib bikini bolo tie bonnet bow tie brassiere bulletproof vest cardigan chest cowboy hat crash helmet dishrag feather boa fur coat gown handkerchief hook hoopskirt jean jersey kimono knee pad lab coat maillot military uniform miniskirt mitten overskirt pajama paper towel poncho sandal sear seat belt shower cap sock sombrero stole suit sweatshirt swimming trunks trench coat velvet vestment wallet wig wool
device	accordion acoustic guitar analog clock assault rifle banjo barometer bassoon binoculars bow buckle bullet train candle car mirror car wheel cash machine cello chime combination lock desktop computer digital clock digital watch disk brake drum drumstick electric fan electric guitar flute gas pump gong hair slide hammer hamper hand-held computer hard disc harmonica harp hatchet horn hourglass laptop lighter loudspeaker loupe magnetic compass maraca marimba maypole microphone missile monitor mouse mousetrap neck brace notebook oboe odometer oil filter organ oxygen mask paddlewheel padlock paintbrush panpipe parking meter pick "potters wheel" projector puck radiator radio telescope remote control revolver rifle safety pin sax scale screen sewing machine ski slide rule slot slug snorkel solar dish space heater speaker web steel drum stethoscope stopwatch strainer sundial sunglass sunglasses switch syringe thresher toaster torch tripod trombone typewriter keyboard upright vending machine violin wall clock whistle
equipment	CD player Polaroid camera balance beam barbells "carpenters kit" cassette player cellular telephone computer keyboard croquet ball crossword puzzle dial telephone drilling platform dumbbell golf ball golfcart horizontal bar iPod jigsaw puzzle modem oscilloscope parachute parallel bars pay-phone photocopy ping-pong ball plate punching bag reel reflex camera soccer ball tape player
establishment	bakery barbershop bookshop butcher shop confectionery shoe shop tobacco shop toyshop
feline	Egyptian cat Persian cat Siamese cat catamount cheetah coil cougar leopard lion panther snow leopard tabby tiger tiger cat
fish	anemone fish barracouta coho eel electric ray gar goldfish great white shark hammerhead lionfish puffer rock beauty stingray sturgeon tench tiger shark
food	French loaf bagel burrito carbonara cheeseburger chocolate sauce consommé cucumber dough egnog espresso guacamole hay hot pot hotdog ice cream ice lolly mashed potato meat loaf pizza potpie pretzel red wine trifle
fruit	Granny Smith acorn buckeye hip jackfruit lemon orange pineapple rapsseed strawberry
furniture	altar barber chair bassinet beaver bookcase china cabinet cradle desk dining table entertainment center file folding chair four-poster medicine chest milk can mink otter park bench pool table rocking chair studio couch table lamp throne toilet seat wardrobe
geological	alp bubble cliff coral reef dome geyser lakeside promontory sandbar seashore valley volcano
insect	ant bee cabbage butterfly cicada cricket damselfly dragonfly dung beetle fly ground beetle lacewing ladybug leaf beetle leafhopper long-horned beetle lycanid mantis monarch peacock rhinoceros beetle ringlet sulphur butterfly tiger beetle walking stick weevil
mammal	African elephant American black bear Angora Arabian camel Indian elephant Madagascar cat Sus scrofa armadillo baboon bighorn bison black-footed ferret brown bear capuchin chimpanzee colobus dugong echidna fish fox squirrel gazelle gibbon gorilla grey whale guenon guinea pig hamster hare hartebeest hippopotamus ibex ice bear impala indri killer whale koala langur lesser panda llama macaque marmoset marmot meerkat mongoose orangutan ox panda patas platypus polecat porcupine proboscis monkey ram sea lion siamang sloth bear spider monkey squirrel monkey three-toed sloth titi tusker wallaby warthog water buffalo wombat wood rabbit zebra
material	chain comet doormat groom knot spindle toilet tissue
musical	grand piano
organism	American lobster Dungeness crab German shepherd admiral agaric badger ballerina barn spider black and gold garden spider black widow bolete boxer brain coral centipede chiton cockroach conch coral fungus crawfish dam ear earthstar fiddler crab flatworm garden spider gyromitra harvester harvestman hen-of-the-woods hermit crab hog howler monkey isopod jellyfish king crab mushroom nematode nipple printer rock crab rule scorpion scuba diver sea cucumber sea slug sea urchin snail spiny lobster starfish stinkhorn tarantula tick trilobite weasel wing wolf spider
plant	acorn squash artichoke banana bell pepper broccoli butternut squash cardoon cauliflower corn custard apple daisy head cabbage ocarina pinwheel pomegranate sea anemone sorrel spaghetti squash "yellow lady slipper" zucchini
reptile	African chameleon African crocodile American alligator American chameleon Gila monster Indian cobra Komodo dragon agama alligator lizard banded gecko boa constrictor box turtle common iguana diamondback frilled lizard grass snake green lizard green mamba green snake hognose snake king snake leatherback turtle loggerhead mud turtle night snake ringneck snake rock python sand viper sea snake sidewinder terrapin thunder snake triceratops vine snake water snake whiptail
sport	baseball basketball football helmet rugby ball tennis ball volleyball
tool	can opener chain saw corkscrew lawn mower letter opener lumbermill nail plane plow plunger power drill screw screwdriver shovel
utensil	Crock Pot caldron coffeepot frying pan spatula teapot wok wooden spoon
vehicle	Model T aircraft engine airliner airship ambulance amphibian balloon barrow beach wagon bicycle-built-for-two bobled cab canoe catamaran chambered nautilus container ship convertible dogsled electric locomotive fire engine fireboat forklift freight car garbage truck go-kart gondola half track horse cart jeep jitriskha lifeboat limousine liner minivan moped motor scooter mountain bike moving van oxcart passenger car pickup pirate racer recreational vehicle shopping cart snowmobile snowplow space shuttle speedboat sports car steam locomotive streetcar submarine tank tow truck tractor trailer truck tricycle trimaran unicycle wagon warplane yawl

Table 3. Mapping between categories from the WordNet Hierarchy and the ImageNet-1k classes used for assigning a category to the concept clusters.

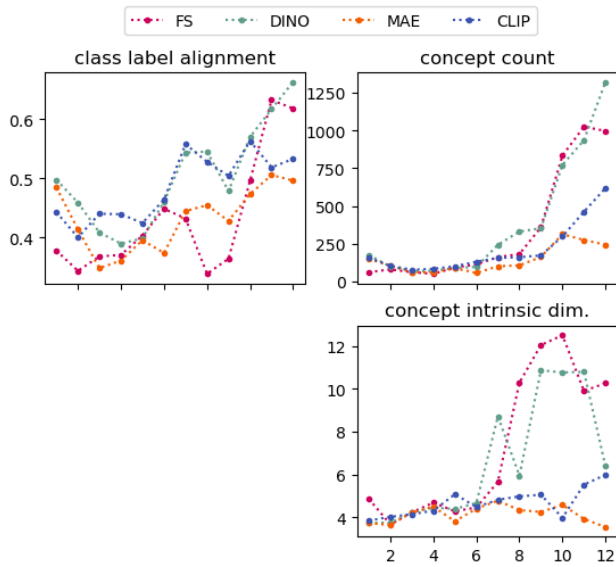


Figure 11. Class label alignment, token location alignment (both based on CBA), concept count, and the average intrinsic dimensionality (based on [12]) across concepts for CLS representations supplement the intra-model alignment analysis, by providing insights into how well the model aligns with ImageNet-1k labels, the spatial organization of tokens, and the complexity of the learned concepts as they evolve through the layers.

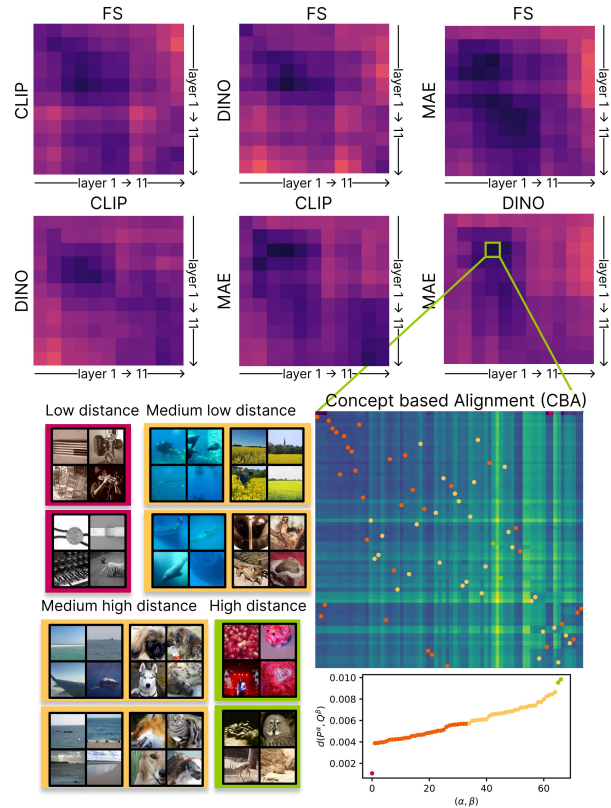


Figure 12. Inter-model relationships based on CLS representations across layers. In the **upper part**, we show CBA to visualize how representations differ between the models (darker pixels correspond to higher alignment). In the **lower part** we zoom in into the concept-wise distances  $d_{cross}(P^\alpha, P^\beta)$  between the representation of in MAE layer 2 and DINO layer 3. We give examples of universal concepts with low distance and unique ones with high distance from matches of pairs that minimize the total distance.





Figure 13. We zoom into the SEQ representations at DINO layer 1 and show a UMAP embedding constructed from the pairwise distance of concepts measured by  $d_{cross}(P^\alpha, P^\beta)$ . Each point in this *concept atlas* corresponds to a distinct concept  $P^\alpha$ . To convey their meaning, we show four random input tokens from the members of the concept cluster  $P^\alpha$ . We dissect the concept atlas into 7 groups and show four random concepts for each group. Concepts representing similar colors lie within the same group, e.g. shades of blue in the blue group or red and orange in the red group.

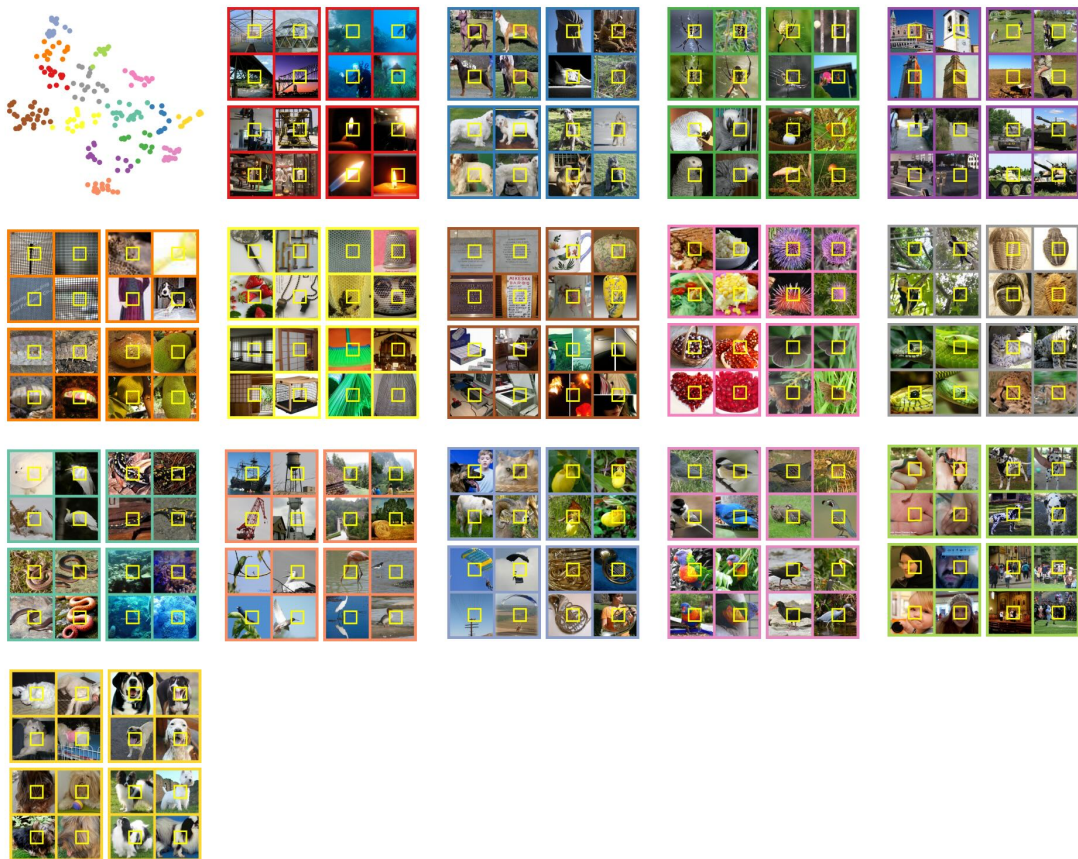


Figure 14. We zoom into the SEQ representations at DINO layer 6 and show a UMAP embedding constructed from the pairwise distance of concepts measured by  $d_{cross}(P^\alpha, P^\beta)$ . Each point in this *concept atlas* corresponds to a distinct concept  $P^\alpha$ . To convey their meaning, we show four random input tokens from the members of the concept cluster  $P^\alpha$ . We dissect the concept atlas into 15 groups and show four random concepts for each group. Most concepts represent a pattern or texture which are similar within each group.

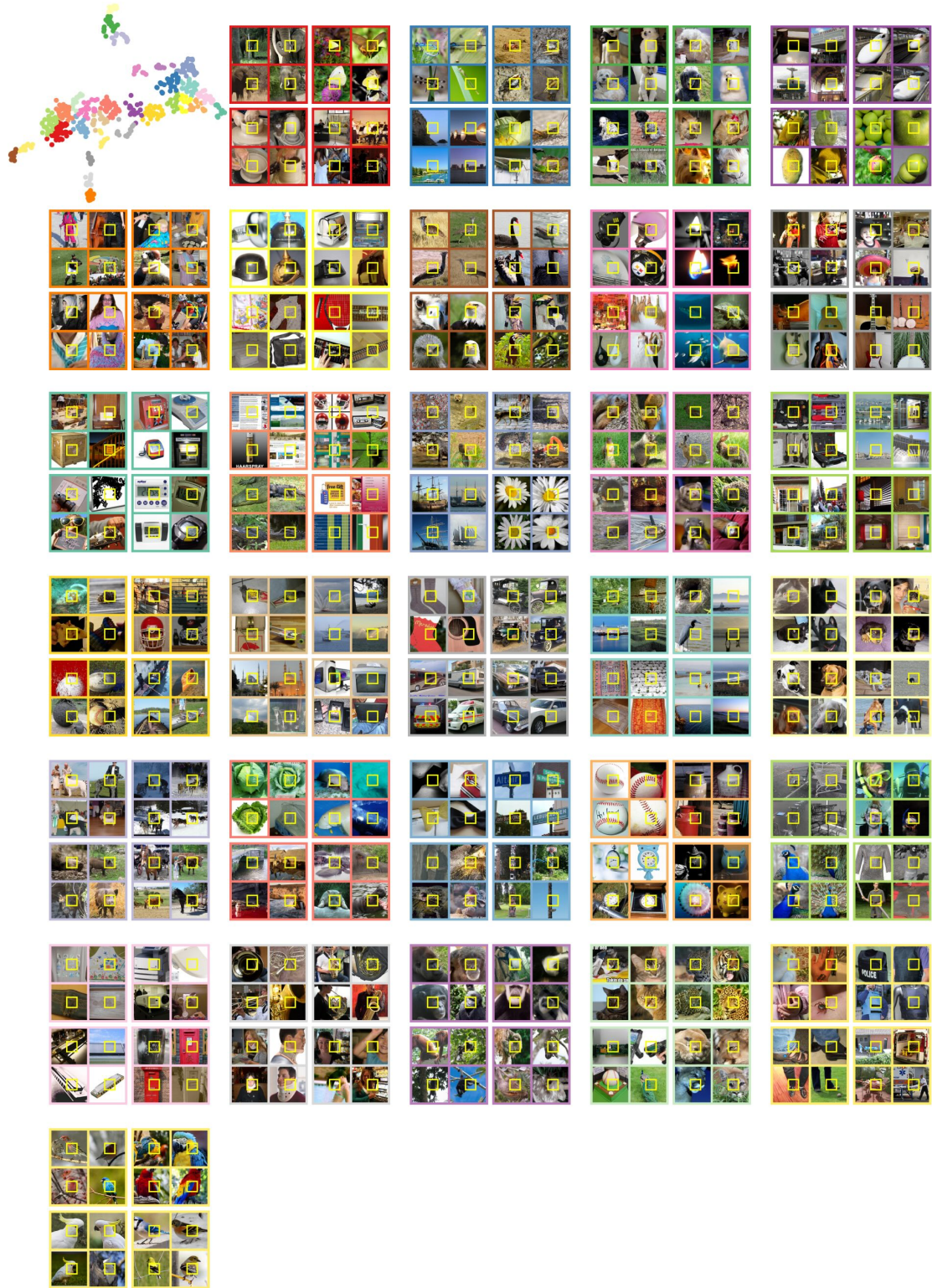


Figure 15. We zoom into the SEQ representations at DINO layer 11 and show a UMAP embedding constructed from the pairwise distance of concepts measured by  $d_{cross}(P^\alpha, P^\beta)$ . Each point in this *concept atlas* corresponds to a distinct concept  $P^\alpha$ . To convey their meaning, we show four random input tokens from the members of the concept cluster  $P^\alpha$ . We dissect the concept atlas into 30 groups and show four random concepts for each group. For most groups, these are semantically similar.

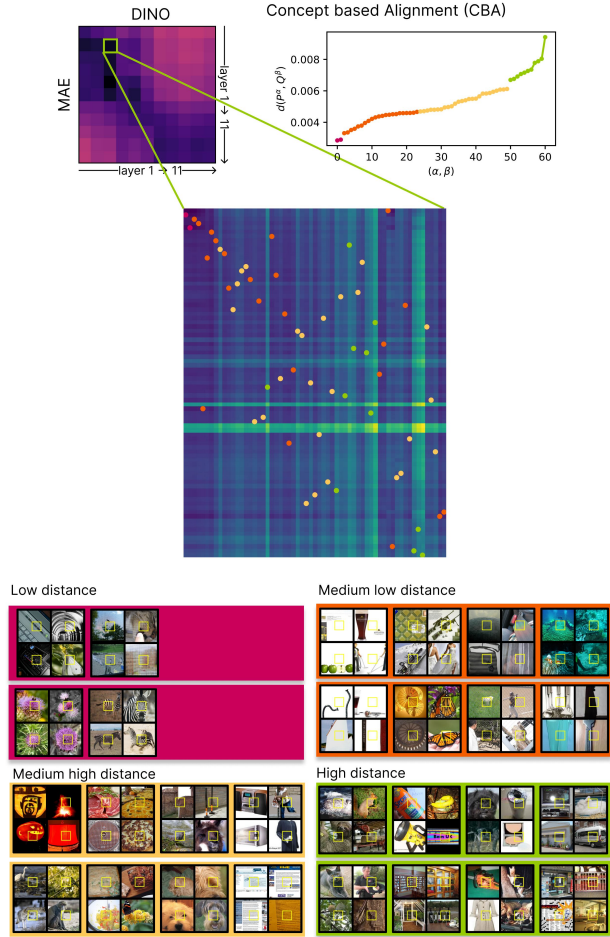


Figure 16. CBA of SEQ concepts across layers of MAE and DINO (darker pixels correspond to higher alignment). We zoom in into the concept-wise distances  $d_{cross}(P^\alpha, P^\beta)$  between the representation of layer 2 in MAE and layer 3 in DINO. We give examples of universal concepts with low distance and unique ones with high distance from matches of pairs that minimize the total distance.

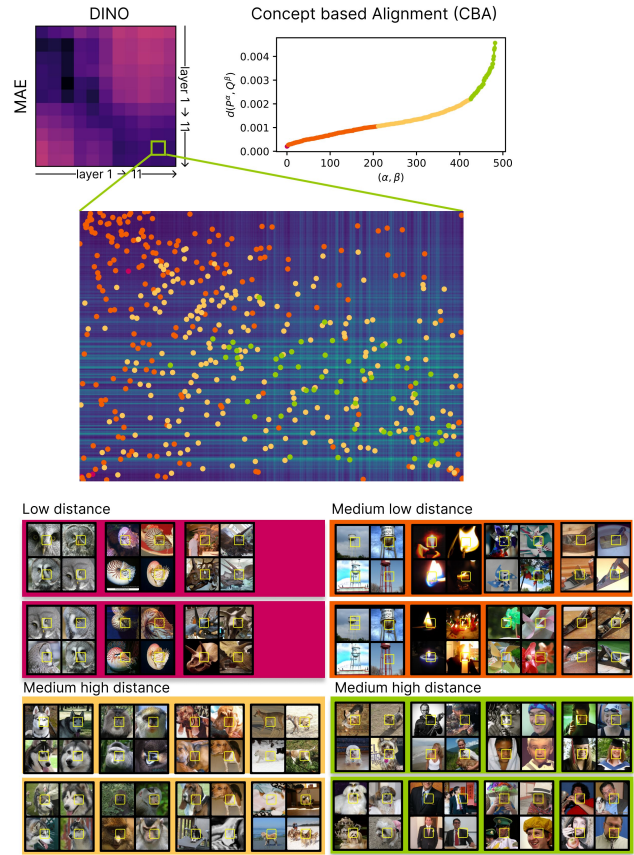


Figure 17. CBA of SEQ concepts across layers of MAE and DINO (darker pixels correspond to higher alignment). We zoom in into the concept-wise distances  $d_{cross}(P^\alpha, P^\beta)$  between the representation of layer ten in MAE and DINO. We give examples of universal concepts with low distance and unique ones with high distance from matches of pairs that minimize the total distance.